Functional & Integrative Genomics (2025) 25:64
https://doi.org/10.1007/s10142-025-01573-6

RESEARCH

Combined transcriptomic and proteomic analyses reveal relevant myelin features in mice with ischemic stroke

Qiuyang Qian[1] · Hao Lyu[2,3] · Wei Wang[1] · Qiwen Wang[1] · Desheng Li[1] · Xiaojia Liu[2] · Yi He[2] · Mei Shen[1]

Received: 1 June 2024 / Revised: 24 February 2025 / Accepted: 5 March 2025

Abstract

Ischemic stroke (IS), a leading cause of global disability and mortality, is characterized by white matter damage and demyelination. Despite advances, the molecular mechanisms driving post-IS myelin pathology remain poorly understood, limiting therapeutic development. This study investigates key myelin-related genes (MRGs) and their regulatory networks to identify novel therapeutic targets. A transient middle cerebral artery occlusion (MCAO) model was established in C57BL/6 mice, with brain tissues collected at four timepoints (Sham0D, MCAO0D, MCAO7D, MCAO14D). Transcriptomic and proteomic sequencing were performed, followed by soft clustering (Mfuzz), functional enrichment (GO/KEGG), and ROC analysis to identify key MRGs. Competing endogenous RNA (ceRNA) networks were constructed, and drug prediction was conducted using the Comparative Toxicogenomics Database (CTD) and molecular docking. Expression validation was performed via qRT-PCR and Western blot. Integrated multi-omics analysis identified *Wasf3* and *Slc25a5* as key MRGs, enriched in mitochondrial respiration, calcium metabolism, and cytoskeletal regulation. The AUC values of the one-to-one model scores were all greater than 0.7, suggesting that *Wasf3* and *Slc25a5* were able to effectively discriminate between samples from different time points. A ceRNA network revealed critical interactions, including the *Wasf3-mmu-miR-423-5p-H19* axis, linking apoptosis and myelin dysfunction. Drug prediction highlighted valproic acid (VPA) as a high-affinity binder for both genes (binding energies: −4.2 and −4.7 kcal/mol), suggesting its potential as a therapeutic candidate for IS. Experimental validation confirmed significant downregulation of *Wasf3* mRNA ($p < 0.01$) and protein ($p = 0.069$) post-IS, while *Slc25a5* showed no significant changes, potentially due to sample size limitations. This study establishes *Wasf3* and *Slc25a5* as pivotal regulators of post-IS myelin pathology and proposes VPA as a promising therapeutic candidate to enhance remyelination. The findings underscore the utility of multi-omics approaches in bridging molecular mechanisms to clinical translation, offering new strategies for IS diagnosis and treatment.

Keywords Ischemic stroke · Myelin-related genes · Transcriptome · Proteomics

Introduction

Ischemic stroke (IS), the most common form of stroke, is one of the leading cause of global disability and mortality. Historically, the pathological mechanisms underlying post-IS dysfunction have been attributed to neuronal loss, cerebral edema, neuroinflammation, and glial scar formation at the infarction site (Du et al. 2022). Corresponding therapeutic strategies have focused on rapid restoration of blood flow through thrombolytic therapy, endovascular thrombectomy, and neuroprotective agents (Paul & Candelario-Jalil 2021). However, emerging evidence highlights that focal ischemic injury triggers secondary global impairments (Veldsman et al. 2018) and multidomain sensorimotor deficits (Corbetta et al. 2018), implicating white matter as a critical

Qiuyang Qian and Hao Lyu are co-first authors.

✉ Mei Shen
meishendrms@outlook.com

[1] Department of Rehabilitation Medicine, People's Hospital of Longhua, No 38 Jinglong Construction Road, Shenzhen 518109, Longhua District, China

[2] Department of Neurosurgery, Shenzhen Second People'S Hospital, First Affiliated Hospital of Shenzhen University, Shenzhen 518000, China

[3] Shenzhen Institute of Advanced Technology, Chinese Academy of Sciences, Shenzhen 518055, China

Published online: 14 March 2025

mediator due to its vulnerability to ischemia. White matter components, i.e. the astrocytes, axons and myelin sheaths, are increasingly recognized as pivotal players in post-IS dysfunction (Li et al. 2020). Among these, demyelination has emerged as a key pathological process contributing to long-term disability. Despite progress, the molecular mechanisms driving myelin damage and repair remain poorly understood, limiting the development of targeted therapies. Understanding the mechanisms driving post-IS dysfunction is essential for refining diagnostic methods and developing novel therapeutic strategies.

Recent studies underscore the significance of white matter demyelination in IS pathophysiology. For instance, Zuo et al. demonstrated that cortical ischemia triggers demyelination in distant, nonischemic areas such as the corpus callosum, suggesting a secondary degenerative process (Zuo et al. 2019). Furthermore, Khodanovich et al. provided longitudinal insights into post-IS myelin dynamics, using magnetic resonance imaging (MRI) to map the spatiotemporal progression of demyelination and remyelination in the striatum of middle cerebral artery occlusion (MCAO) models across acute to chronic phases (Khodanovich et al. 2021). While these studies, along with others, confirm global white matter alterations after IS, they collectively underscore a critical gap: the mechanisms governing myelin damage and repair as well as their precise role in IS pathology remain poorly defined (Raffaele & Fumagalli 2022). This knowledge gap limits the development of therapies targeting white matter restoration, a key determinant of functional recovery.

In recent years, advances in omics technologies have revolutionized the exploration of molecular mechanisms underlying complex diseases (Ghosh et al. 2018). Transcriptomics and proteomics, as complementary approaches, provide distinct yet interconnected insights: transcriptomics captures upstream regulatory dynamics, including transcriptional and post-transcriptional modifications (Zhang et al. 2019), while proteomics reflects downstream functional protein expression and activity (Hochrainer & Yang 2022). However, the pathophysiological complexity of IS, which is driven by multilayered molecular interactions, cannot be fully deciphered through single-omics analyses (Rojahn et al. 2020). Integrating multi-omics data bridges this gap, enabling a holistic view of gene expression from RNA to protein and unraveling regulatory networks across biological hierarchies. For instance, Song and colleagues combined transcriptomic and proteomic profiling to uncover RAD52's dual roles in DNA repair and metabolic regulation, linking its activity to neurodegenerative pathways (Song et al. 2025). Their work identified Bhmt1b as a therapeutic target, demonstrating how multi-omics integration connects molecular mechanisms to phenotypic outcomes. Similarly, Bae et al. fused MRI imaging biomarkers with transcriptomic and proteomic data, revealing molecular pathways underpinning cerebral aging and validating imaging markers for neurodegenerative diseases like Alzheimer's (Bae et al. 2025). In IS specifically, integrated transcriptomic and proteomic analyses have identified novel biomarkers (Li et al. 2022a, b, c) and elucidated the neuroprotective mechanisms of Yiqi Tongluo Granules, accelerating their clinical translation (Yuan et al. 2023). These studies exemplify how multi-omics strategies synergize macroscopic observations with molecular insights, offering a framework to dissect systemic interactions across biological scales. By mapping such networks, multi-omics approaches hold immense potential to elucidate IS pathogenesis, pinpoint therapeutic targets, and accelerate biomarker discovery. This paradigm shift promises to transform our understanding of myelin-related pathology in IS, bridging mechanistic gaps that single-omics studies cannot address (Montaner et al. 2020).

In summary, while prior studies have established the significance of white matter demyelination in IS, critical gaps persist in understanding the molecular orchestration of myelin damage and repair. First, existing research lacks a comprehensive exploration of the dynamic multi-omics regulatory networks governing post-IS myelin pathology. Second, the role of myelin-related genes (MRGs) in disease progression, functional recovery, and their cross-disease relevance in cerebrovascular disorders remains underexplored. These limitations impede the translation of mechanistic insights into targeted therapies for white matter restoration, a critical determinant of functional recovery after IS. To address these challenges, this study integrates transcriptomic and proteomic profiling with experimental validation to identify key MRGs driving IS pathophysiology. We elucidate their regulatory mechanisms and map their associations with other cerebrovascular diseases, Additionally, we predict therapeutic compounds targeting these genes. By bridging multi-omics data with functional outcomes, our work not only advances the understanding of myelin-related pathology in IS but also establishes a framework for biomarker discovery and therapeutic development. These findings provide actionable insights into prognosis prediction and the design of novel strategies for white matter repair, underscoring the transformative potential of multi-omics approaches in overcoming the limitations of conventional single-omics studies.

Material and methods

Animal model and tissue collection

All experimental procedures were conducted in accordance with protocols approved by the Experimental Animal Ethics Committee of Shenzhen Longhua People's Hospital (Approval No. LHRY-2106002) and Wuhan Servicebio Technology Co., Ltd. (Approval No. 2022002). Adult

male C57BL/6 mice (8–10 weeks old, weighing 25–28 g) were used in this study. The animals were housed in a controlled environment with a 12-hour light–dark cycle, maintaining a temperature of approximately 22°C and humidity between 45% and 50%.

Transient MCAO was induced in mice to construct IS model, as previously described by Chen et al. (Chen et al. 2020). Briefly, anesthesia was initiated with 5% isoflurane and maintained at 1%. A midline neck incision exposed the left common carotid artery (CCA), external carotid artery (ECA), and internal carotid artery (ICA). The ECA and its superior thyroid branch were electrocoagulated, and a 6-0 silicone-coated monofilament was advanced into the ICA to occlude the MCA origin for 90 minutes. Post-surgery, mice recovered in a 32°C incubator. Sham controls underwent identical procedures without filament insertion.

Infarct volume was quantified 24 hours post-MCAO using 2,3,5-triphenyltetrazolium chloride (TTC) staining. The IS group exhibited a mean infarct volume of 40±10%, while no infarction was observed in sham controls. Power analysis ($\alpha = 0.05$, power = 0.8) indicated a minimum sample size of 1 per group to detect significant differences, consistent with prior studies. Based on methodological rigor and literature precedent (Li et al. 2017; Meng et al. 2023), final group sizes were set to 24(MCAO) and 10 (sham).

We further established one sham control group and three MCAO experimental groups with different onset times, i.e. Sham0D group: Sham surgery, sacrificed immediately; MCAO0D group: MCAO surgery, sacrificed immediately; MCAO7D group: MCAO surgery, sacrificed 7 days post-occlusion; and MCAO14D group: MCAO surgery, sacrificed 14 days post-occlusion. At designated timepoints, mice were euthanized via anesthetic overdose, and ipsilateral brain hemispheres were rapidly dissected on ice for transcriptomic and proteomic analyses.

RNA sequencing

RNA sequencing was performed by BGI Genomics (Shenzhen, China). Total RNA was extracted from the brain samples of 24 mice using TRIzol reagent (Invitrogen, Carlsbad, CA, USA). RNA concentration and purity were assessed using an Agilent 2100 Bioanalyzer (Agilent Technologies, Santa Clara, CA, USA), and RNA integrity was evaluated through agarose gel electrophoresis with ethidium bromide staining. RNA libraries were constructed using the MGIEasy RNA directional library preparation kit (BGI Genomics) and sequenced on the BGI DNBSEQ sequencing platform (BGI Genomics).

Protein sequencing

Proteome sequencing was conducted by Shanghai Applied Protein Technology Co., Ltd. (APTBIO, Shanghai, China). Samples were homogenized using an MP FastPrep-24 homogenizer (MP Biomedicals, Santa Ana, CA, USA), and protein digestion was performed via the filter-aided sample preparation (FASP) method using the Thermo ScientificTM PierceTM High pH Reversed-Phase Peptide Fractionation Kit. The iRT Kit (Biognosys, MA, USA) peptides were spiked prior to data-dependent acquisition (DDA) analysis. The fractions were then analyzed using a Thermo Scientific Q-Exactive HF-X mass spectrometer connected to an Easy-nLC 1200 chromatography system (Thermo Scientific, Waltham, MA, USA) to generate the DDA library. Peptides from each sample were further analyzed in data-independent acquisition (DIA) mode. DIA data analysis and database searching were performed using SpectronautTM 14.4.200727.47784 (Biognosys) software.

Soft clustering analysis and enrichment analysis

Mfuzz identifies time series expression patterns and clusters genes with similar expression profiles to understand their dynamic behavior and functional relationships (Futschik & Carlisle 2005). To analyze the temporal expression trends of proteins and RNA, the fuzzy C-means clustering algorithm in Mfuzz (v2.60.0; data of use: 2023.12.5) was employed to classify and cluster genes or proteins with similar expression patterns across four groups (Sham0D, MCAO0D, MCAO7D, and MCAO14D). The algorithm used traditional methods to achieve clustering by calculating membership degrees and cluster centers, with the expected number of clusters set to 10. Gene Ontology (GO) and Kyoto Encyclopedia of Genes and Genomes (KEGG) enrichment analyses were then performed using clusterProfiler (v4.8.2; data of use: 2023.12.5), with org.Mm.eg.db (v3.17.0; data of use: 2023.12.5) as the background gene set. Enrichment was focused on common trend genes exhibiting different expression patterns in both the transcriptome and proteome (p adjust < 0.05, count > 2) (Wu et al. 2021). Expression patterns enriched in myelin-associated pathways were identified in both transcriptomic and proteomic data. The intersection of these myelin-related genes was then obtained, revealing common myelin-associated genes across both datasets.

Identification and enrichment analysis of key genes

To assess the ability of the intersecting myelin genes to differentiate samples obtained at different time points, a generalized linear model was constructed using the R package pROC (v1.18.4; data of use: 2023.12.5) to predict sample classification based on these genes. The receiver operating

characteristic (ROC) curve for prediction probabilities was generated for both transcriptomic and proteomic datasets (Robin et al. 2011). Genes and proteins with an area under the curve (AUC) value greater than 0.7 were considered key genes. Gene set enrichment analysis (GSEA) was then performed using clusterProfiler (v4.8.2; data of use: 2023.12.5) to explore the functions and pathways of these key genes. Using org.Mm.eg.db as the default background gene set, correlations between key genes and other genes were calculated in the transcriptome data and ranked in descending order. Single-gene GSEA, including GO and KEGG analyses, was conducted with significance thresholds set at p adjust < 0.05 and q-value < 0.2.

Colocalization analysis and GeneMANIA analysis

The subcellular localization of the protein products of the key genes was predicted using mRNALocater (http://bio-bigdata.cn/mRNALocator). Key gene interactions and their functional relationships were explored using GeneMANIA (https://genemania.org/).

Single-sample GSEA (ssGSEA)

Next, ssGSEA in GSVA (v1.48.2; data of use: 2023.12.5) was utilized to evaluate characteristic gene sets from the Molecular Signatures Database (MSigDB, https://www.gsea-msigdb.org/gsea/msigdb/index.jsp) (Hänzelmann et al. 2013), focusing on differences in immune regulation, exosome activity, mitochondrial function, and copper–iron–calcium ion metabolism across the onset-time-based groups. The ssGSEA algorithm was applied to calculate the gene set scores for the transcriptomes and proteomes, and the limma package (v3.54.2; data of use: 2023.12.5) was used to identify gene sets exhibiting significant differences between the groups (Ritchie et al. 2015). Next, the R package ggplot2 (v3.4.2; data of use: 2023.12.5) was used to create bar plots of differential functions. Genes were considered upregulated if $t > 0$ and downregulated if $t < 0$. Additionally, ComplexHeatmap (v2.14.0; data of use: 2023.12.5) was employed to generate heat maps of the ssGSEA scores, visualizing immune response process differences across samples (Gu et al. 2016).

Regulatory mechanisms

To elucidate the regulatory mechanisms of key genes in mouse IS, transcription factors (TFs) corresponding to the key genes were predicted using the NetworkAnalyst database (https://www.networkanalyst.ca/), and TF–mRNA networks were constructed. Additionally, competing endogenous RNA (ceRNA) networks were built for circRNA–miRNA–mRNA and lncRNA–miRNA–mRNA analyses. The network diagrams were visualized using Cytoscape (v3.8.2; data of use: 2023.12.6).

Differentially expressed (DE) lncRNAs and DE-circRNAs between MCAO and control samples were identified using DESeq2 (v1.36.0; data of use: 2023.12.6) (Love et al. 2014), with screening criteria set as $|\log2FC| > 0.5$ and $p < 0.05$. Volcano plots and heatmaps of DE-lncRNAs and DE-circRNAs were generated using ggplot2 (v3.4.2; data of use: 2023.12.6) and ComplexHeatmap (v2.14.0; data of use: 2023.12.6), respectively (Wang et al. 2022). Potential miRNAs targeting the key genes and lncRNAs were predicted using the starBase database (https://starbase.sysu.edu.cn/), and the intersection of potential lncRNAs with DE-lncRNAs was used to identify key lncRNAs. Following this, miRNAs targeting both mRNA and lncRNA were intersected to identify co-regulated miRNAs, and an mRNA–miRNA–lncRNA regulatory network was constructed. Similarly, potential circRNAs associated with the targeted miRNAs were predicted *via* starBase, and the intersection of potential circRNAs with DE-circRNAs was used to identify key circRNAs. The mRNA-targeting miRNAs and circRNA-targeting miRNAs were intersected to identify co-regulated miRNAs, leading to the construction of the mRNA–miRNA–circRNA regulatory network. Finally, the network was beautified using Cytoscape (v3.8.2; data of use: 2023.12.6).

Drug prediction and molecular docking

To investigate the roles of the identified key genes in other cerebrovascular diseases, associations between the genes and cerebrovascular diseases were analyzed using the Comparative Toxicogenomics Database (CTD, http://ctdbase.org/). This database was also used to identify drugs targeting the key genes and to construct gene–drug network, which was visualized using Cytoscape (v3.8.2; data of use: 2023.12.6) software. Subsequently, the drug with the highest binding affinity to the key genes was selected for molecular docking. The two-dimensional (2D) structures of these drugs were downloaded from the PubChem database (https://pubchem.ncbi.nlm.nih.gov) and adjusted to their energy-minimized conformations using ChemOffice 2021. The protein crystallographic data for the targets were obtained from the Protein Data Bank (PDB, https://www.rcsb.org/). Molecular docking was then performed using AutoDock Vina (v1.1.2; data of use: 2023.12.6) (Trott and Olson 2010) with docking binding energies less than −1.2 kcal/mol considered indicative of feasible binding.

Expression validation of the MRGs

In this study, quantitative real-time polymerase chain reaction (qRT-PCR) and Western blotting (WB) were used to

verify the expression of the MRGs screened out in the previous stages.

qRT-PCR Protocol. First, total RNA is extracted from tissue using a grinding buffer and homogenization. The lysate is centrifuged, mixed with chloroform substitute and isopropanol, and incubated to precipitate RNA. After washing and drying, RNA is dissolved, quantified, and adjusted to 200 ng/μL.Then, reverse transcription is performed by mixing RNA with gDNA remover and reverse transcriptase. The reaction is run at 25°C (gDNA removal), 42°C (cDNA synthesis), and 85°C (enzyme inactivation).Next, quantitative PCR is set up with SYBR Green Master Mix, primers, and cDNA. Triplicate reactions are amplified for 40 cycles with melt curve analysis. Finally, data is analyzed using the ΔΔCT method to calculate relative gene expression normalized to a housekeeping gene.

Western Blot Protocol. First, proteins are extracted from cells or tissues using RIPA buffer containing protease inhibitors. For cells, adherent cultures are washed and lysed directly, while suspension cells are centrifuged and resuspended in lysis buffer. Tissues are homogenized with grinding beads. The lysates are then incubated on ice, centrifuged, and supernatants collected. Protein concentration is optionally quantified via a BCA assay. Next, samples are denatured by heating with a reducing buffer and stored at −20°C or −80°C. Then, SDS-PAGE gels are prepared by casting resolving and stacking layers. Protein samples are loaded onto the gel and separated by electrophoresis at 200V until the dye front nears the gel bottom. Separated proteins are transferred to a PVDF membrane using a wet transfer system at 300mA for 30 minutes. The membrane is activated in ethanol and carefully assembled into a transfer stack to ensure proper adhesion. Finally, the membrane is blocked with 5% skim milk to prevent nonspecific binding. It is incubated overnight with primary antibodies at 4°C, washed, and treated with a secondary antibody for 30 minutes at room temperature. After final washes, chemiluminescent detection is performed using ECL reagent. Band intensities are analyzed with AIWBwellTM software, which automates orientation correction, molecular weight calibration, and quantifies relative protein levels by normalizing target signals to loading controls.

Statistical analysis

All analyses were conducted using R (v1.1.2; data of use: 2023.12.7), with $p < 0.05$ considered statistically significant. The Benjamini-Hochberg (BH) method was one of the commonly used approaches to control the false discovery rate (FDR). By setting p.adj < 0.05 and q.value < 0.2, FDR control was ensured at the preset level (Xie et al. 2024). This method avoided the overly strict Bonferroni correction while balancing false positives and false negatives.

Results

Identification of 569 common trend genes and 15 key genes using soft cluster analysis

The gene expression matrix and protein expression profile were analyzed using Mfuzz, which yielded 10 distinct clusters as shown in Fig. 1A–B. Transcriptome Cluster 1 and proteome Cluster 5 exhibited an initial increase in expression on day 0 of IS, followed by a decrease from day 0 to day 14. Conversely, transcriptome Clusters 3 and 10, as well as proteome Cluster 8, showed upregulation from day 0 to day 7 of IS, with gradual normalization from day 7 to day 14. Additionally, transcriptome Cluster 9 and proteome Cluster 9 were downregulated on day 0 and progressively normalized from day 0 to day 14. As shown in Fig. 1C and Table S1, the transcriptome GO analysis revealed that Clusters 1, 6, and 9 were enriched in processes related to myelin formation, myelin maintenance, and dense myelin. The proteome GO analysis showed that Clusters 1–7 and Cluster 9 were enriched in the myelin sheath, while Clusters 2, 3, 5, 6, 9, and 10 were enriched in myelin formation, assembly, central nervous system myelination, peripheral nervous system myelination, myelin maintenance, dense myelin, and structural components of myelin. The results were shown in Fig. 1D and Table S2. In Fig. 1E–F, both transcriptome Cluster 9 and proteome Cluster 9 were predominantly associated with the cellular component and biological process of myelin formation, exhibiting similar expression trends. Consequently, the enriched myelin-related pathways identified two overlapping myelin genes, *Wasf3* and *Slc25a5* as shown in Fig. 1G.

Identification and correlation analysis of *Wasf3* and *Slc25a5*

ROC curves in Fig. 2A–B demonstrated that the AUC values for the final OvO model scores from both the transcriptome and proteome exceeded 0.7, indicating that *Wasf3* and *Slc25a5* effectively distinguished samples from different time points. These two genes were selected as key genes for further analysis. The GO results for the key genes showed enrichment in mitochondrial protein-containing complexes, inner mitochondrial membrane protein complexes, and the mitochondrial respirasome as shown in Fig. 2C, E. Additionally, the KEGG analysis in Fig. 2D, F revealed that *Wasf3* and *Slc25a5* were primarily enriched in five pathways: oxidative phosphorylation (Mus musculus), citrate cycle (TCA cycle) (Mus musculus), Parkinson's disease (Mus musculus), diabetic cardiomyopathy (Mus musculus), and Huntington's disease (Mus musculus).

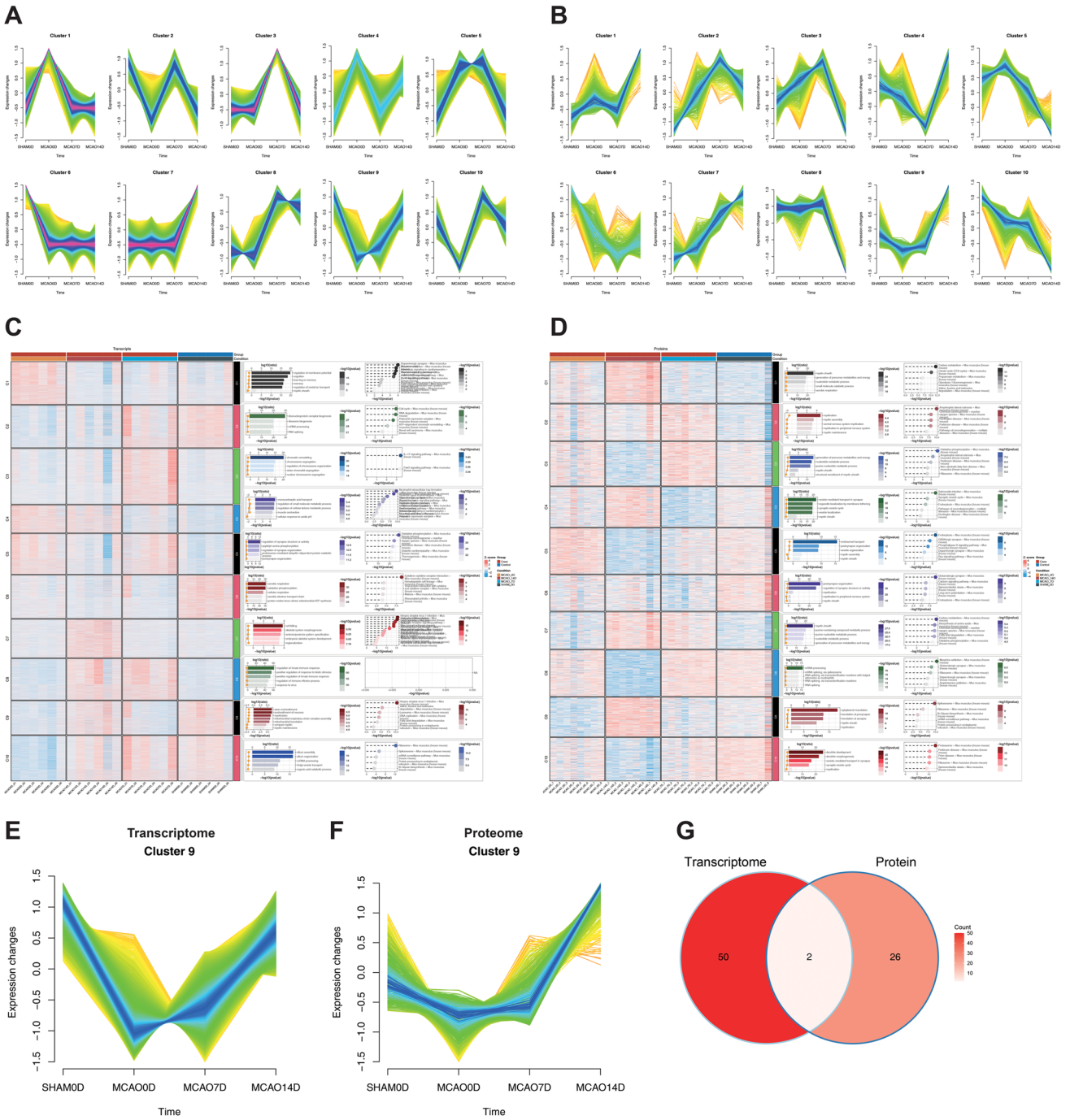

Fig. 1 Gene enrichment analysis of common trends across time series. **A.** Transcriptome clustering; The yellow and green lines corresponded to genes with low membership values, while the red and blue lines corresponded to genes with high membership values; **B.** Proteome clustering; The yellow and green lines corresponded to proteins with low membership values, while the red and blue lines corresponded to proteins with high membership values; **C-D.** Transcriptome and proteome enrichment results: X-axis represents gene ratio; bubble size indicates the number of enriched targets; bubble color reflects P-value; **E–F.** Cluster 9 analysis of transcriptome and proteome; **G.** Myelin-related intersection genes in transcriptome and proteome Cluster 9

Localization of the protein products of the key genes in the nucleus and their relationships with multiple genes

Co-localization analysis indicated that the products of *Wasf3* and *Slc25a5* predominantly localized to the nucleus as shown in Fig. 3A. Additionally, these key genes exhibited strong associations with others, such as Actr3, Jmy, Wast2, and Whamm, and were implicated in several processes, including the positive regulation of actin filament polymerization, protein polymerization, and actin filament regulation as shown in Fig. 3B.

Differences in various pathways between the onset-time-based groups

Further analysis of immune regulation, exosome activity, mitochondrial function, and copper–iron–calcium ion metabolism in characteristic gene sets revealed distinct differences between groups stratified by onset time. As shown in Fig. 4A–F, in the proteome, WP iron homeostasis was significantly activated in the MCAO7D group compared to MCAO0D and Sham0D groups, while it was notably suppressed in the MCAO14D group relative to MCAO7D. In the transcriptome, the negative regulation of calcium ion transmembrane channels was significantly inhibited across several groups, including MCAO14D-MCAO7D, MCAO14D-Sham0D, and MCAO0D-Sham0D, whereas iron ion homeostasis and transport were prominently upregulated in both MCAO7D-MCAO0D and MCAO7D-Sham0D groups as shown in Fig. 5A–F. These results suggest that the identified functions and pathways exert distinct roles across the groups defined by onset time.

Complex regulatory mechanisms of the key genes in IS

TFs corresponding to the two key genes were predicted using the NetworkAnalyst database. As shown in Fig. 6A, seven TFs were identified for *Slc25a5*, whereas no TFs were associated with *Wasf3*. The correlation networks of *Slc25a5* with the seven TFs, including *Slc25a5–UBTF* and *Slc25a5–TCF12*, were then constructed. In Fig. 6B–C, a total of 123 DE-lncRNAs were identified between the MCAO and control groups, with 98 upregulated in the MCAO samples and 15 downregulated in the control samples. Additionally, *Slc25a5* was predicted to target 9 miRNAs, while *Wasf3* targeted 23 miRNAs. A total of 936 miRNA-targeted lncRNAs were predicted using the starbase database, and 8 key lncRNAs were obtained by intersecting the 123 DE-lncRNAs with the 936 targeted lncRNAs as shown in Fig. 6D. This led to the identification of a regulatory network comprising 2 mRNAs, 11 miRNAs, and 8 lncRNAs, including the *Wasf3–mmu-miR-882–H19* and *Slc25a5–mmu-miR-137-3p–4930403D09Rik* axes as shown in Fig. 6E. Similarly, in Fig. 7A–B, 188 DE-circRNAs were identified, with 175 upregulated in the MCAO samples and 13 downregulated in the control samples. As shown in Fig. 7C, a total of 594 miRNA-targeted circRNAs were retrieved, and 7 key circRNAs were selected based on the overlap between the 594 targeted circRNAs and the 188 DE-circRNAs. Furthermore, 18 miRNAs co-regulated by mRNAs and circRNAs were identified. As shown in Fig. 7D, a 2 mRNA–18 miRNA–7 circRNA regulatory network was constructed, which included the *Wasf3–mmu-miR-741-3p–mmu-circ-0000670* and *Slc25a5–mmu-miR-669e-5p–mmu-circ- 0001783* axes, highlighting the complex regulatory interactions.

Prediction of 243 key gene-related drugs with potential therapeutic effects on IS

The role of key genes in other cerebrovascular diseases was further investigated. Figure 8A presented the top five cerebrovascular diseases with the highest interaction scores for the key genes. *Slc25a5* exhibited the strongest interaction with stroke, while *Wasf3* also showed a notable interaction with this condition. In addition, both genes were associated with cerebral infarction, cerebral hemorrhage, and IS. A search through the CTD database identified 243 compounds linked to *Wasf3* and *Slc25a5*, including doxorubicin as shown in Table S3 and Fig. 8B. Among these, valproic acid (VPA) exhibited the strongest predicted association with the key genes. The 2D structures of potential drug candidates were downloaded from the PubChem database and optimized to energy-minimized conformations using ChemOffice 2021. Protein molecular crystal structures of the targets were retrieved from the PDB database (https://www.rcsb.org/). Table 1 and Fig. 8C showed that molecular docking of VPA with the two key genes was then performed using AutoDock vina, revealing binding energies of −4.2 and −4.7 kcal/mol for both genes, respectively. In the molecular docking simulation between *Slc25a5* and VPA, hydrogen bonds were formed between serine (SER) at position 180 and arginine (ARG) at position 235 of *Slc25a5* with VPA. In the molecular docking simulation between *Wasf3* and VPA, hydrogen bonds were formed between lysine (LYS) at position 149, aspartic acid (ASP) at position 153, and arginine (ARG) at position 440 of *Wasf3* with VPA. These results suggest that both genes exhibit strong binding affinity for VPA, indicating its potential as a therapeutic agent for IS.

Expression validation of the two key genes after IS

Figure 9 presented the mRNA and protein expression levels of the two key genes (*Wasf3* and *Slc25a5*) were compared between the Sham0D and MCAO7D groups using qRT-PCR

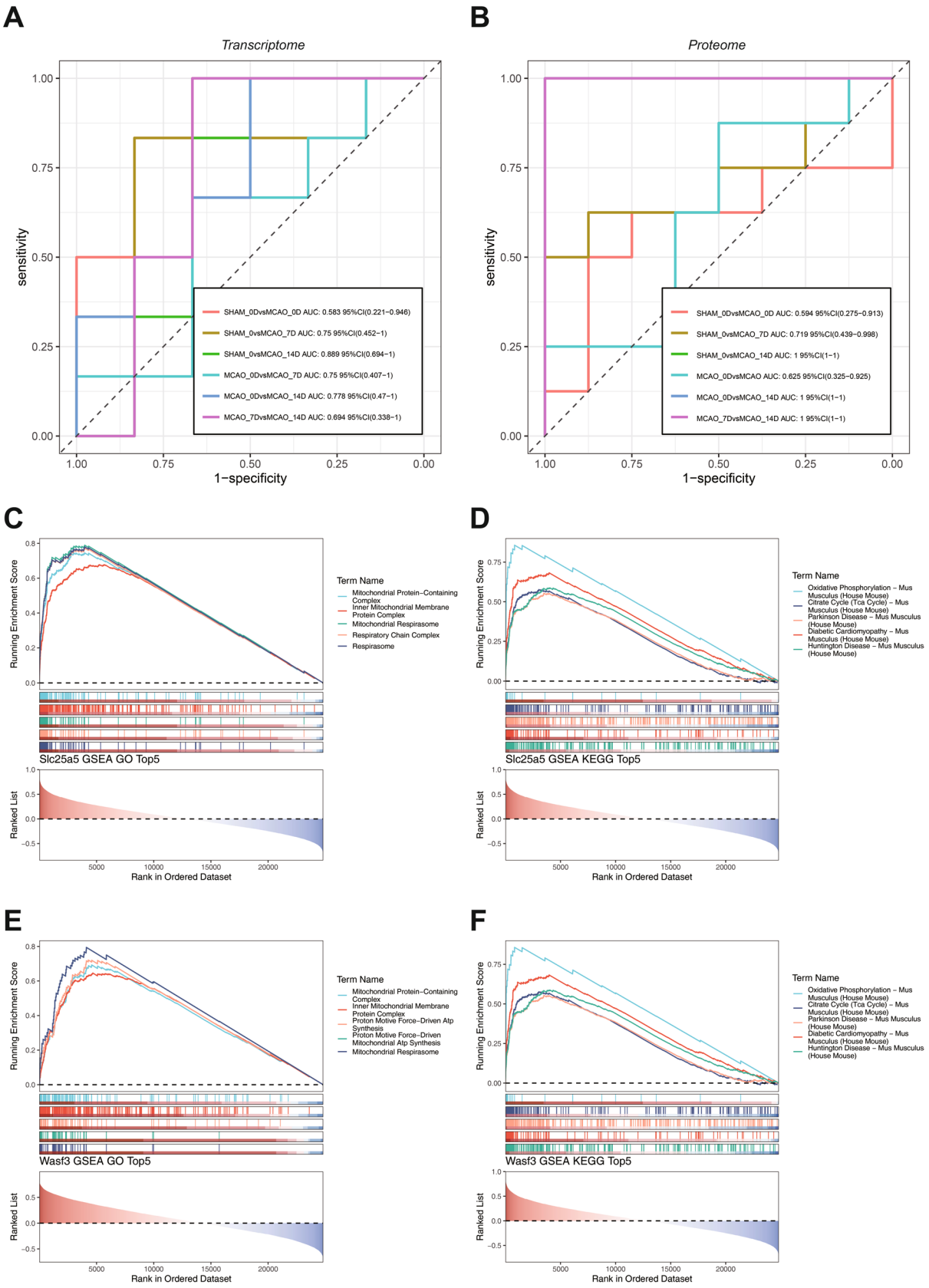
A
Transcriptome
sensitivity
1−specificity
SHAM_0DvsMCAO_0D AUC: 0.583 95%CI(0.221−0.946)
SHAM_0vsMCAO_7D AUC: 0.75 95%CI(0.452−1)
SHAM_0vsMCAO_14D AUC: 0.889 95%CI(0.694−1)
MCAO_0DvsMCAO_7D AUC: 0.75 95%CI(0.407−1)
MCAO_0DvsMCAO_14D AUC: 0.778 95%CI(0.47−1)
MCAO_7DvsMCAO_14D AUC: 0.694 95%CI(0.338−1)
B
Proteome
sensitivity
1−specificity
SHAM_0DvsMCAO_0D AUC: 0.594 95%CI(0.275−0.913)
SHAM_0vsMCAO_7D AUC: 0.719 95%CI(0.439−0.998)
SHAM_0vsMCAO_14D AUC: 1 95%CI(1−1)
MCAO_0DvsMCAO AUC: 0.625 95%CI(0.325−0.925)
MCAO_0DvsMCAO_14D AUC: 1 95%CI(1−1)
MCAO_7DvsMCAO_14D AUC: 1 95%CI(1−1)
C
Running Enrichment Score
Term Name
Mitochondrial Protein−Containing Complex
Inner Mitochondrial Membrane Protein Complex
Mitochondrial Respirasome
Respiratory Chain Complex
Respirasome
Slc25a5 GSEA GO Top5
Ranked List
Rank in Ordered Dataset
D
Running Enrichment Score
Term Name
Oxidative Phosphorylation − Mus Musculus (House Mouse)
Citrate Cycle (Tca Cycle) − Mus Musculus (House Mouse)
Parkinson Disease − Mus Musculus (House Mouse)
Diabetic Cardiomyopathy − Mus Musculus (House Mouse)
Huntington Disease − Mus Musculus (House Mouse)
Slc25a5 GSEA KEGG Top5
Ranked List
Rank in Ordered Dataset
E
Running Enrichment Score
Term Name
Mitochondrial Protein−Containing Complex
Inner Mitochondrial Membrane Protein Complex
Proton Motive Force−Driven Atp Synthesis
Proton Motive Force−Driven Mitochondrial Atp Synthesis
Mitochondrial Respirasome
Wasf3 GSEA GO Top5
Ranked List
Rank in Ordered Dataset
F
Running Enrichment Score
Term Name
Oxidative Phosphorylation − Mus Musculus (House Mouse)
Citrate Cycle (Tca Cycle) − Mus Musculus (House Mouse)
Parkinson Disease − Mus Musculus (House Mouse)
Diabetic Cardiomyopathy − Mus Musculus (House Mouse)
Huntington Disease − Mus Musculus (House Mouse)
Wasf3 GSEA KEGG Top5
Ranked List
Rank in Ordered Dataset

◂**Fig. 2** ROC curve evaluating the diagnostic effect and GSEA results. **A.** One-vs-one (OvO) ROC curve and area under the curve (AUC) for transcriptome data; **B.** OvO ROC curve and AUC for proteome data; **C-D.** GO and KEGG GSEA enrichment results for Wasf3 gene; **E–F.** GO and KEGG GSEA enrichment results for Slc25a5 gene

and WB analysis, respectively. qRT-PCR analysis in Fig. 9A showed that the mRNA expression levels of *Wasf3* and *Slc25a5* were lower in MCAO7D samples compared to Sham0D samples, with a significant decrease observed only for *Wasf3* (*Wasf3*: $p < 0.01$, independent-samples Student's t-test; *Slc25a5*: $p = 0.959$, independent-samples Student's t-test). WB analysis in Fig. 9B and C further confirmed that the protein expression levels of *Wasf3* and *Slc25a5* were reduced in MCAO7D samples compared to Sham0D samples, although the reductions were not statistically significant (*Wasf3*: $p = 0.069$, independent-samples Student's t-test; *Slc25a5*: $p = 0.853$, independent-samples Student's t-test). In this study, *Slc25a5* showed no significant changes in qRT-PCR or WB analyses, likely due to an insufficient sample size to detect subtle expression differences. Future studies could explore its potential under alternative conditions or experimental setups.

Discussion

The white matter, essential for interregional brain communication, exhibits heightened vulnerability to ischemic injury compared to gray matter, a phenomenon exacerbated by its metabolic demands and susceptibility to oxidative stress (Y. Li et al. 2022a, b, c; Singh et al. 2018). A previous study observed a weakening of corticomuscular coupling rhythms in patients with stroke (Guo et al. 2020), which mirrors findings in patients with multiple sclerosis (MS) (Stefancin et al. 2019). Both patients with IS and patients with MS experience similar motor dysfunctions, largely due to white matter demyelination (Edwards et al. 2022). However, effective strategies for myelin protection and repair in the context of post-stroke motor dysfunction remain limited, and the mechanisms underlying demyelination and myelin repair after IS are still poorly understood.

The advent of high-throughput sequencing technologies has propelled transcriptomics and genomics to the forefront of biomedical research. However, while single-omics approaches provide valuable insights, their limitations in capturing the complexity of diseases like IS are increasingly apparent. Multi-omics integration, by contrast, bridges these gaps, offering a systems-level perspective that links molecular interactions to functional outcomes (Chung & Kang 2019). In this study, combining transcriptomic and proteomic analyses identified *Wasf3* and *Slc25a5* as critical mediators of myelin pathology post-IS. *Wasf3* (NCBI database, Gene ID: 10810), a cytoskeletal regulator within the Wiskott–Aldrich syndrome protein family, orchestrates actin dynamics and mitochondrial respiration (Suetsugu et al. 1999). Wang et al. further implicated *Wasf3* in endoplasmic reticulum stress and mitochondrial dysfunction, highlighting its broad regulatory influence across cell types (Wang et al. 2023). Similarly, *Slc25a5* (NCBI database, Gene ID: 292), an ADP/ATP antiporter on the mitochondrial inner membrane, regulates cellular energy

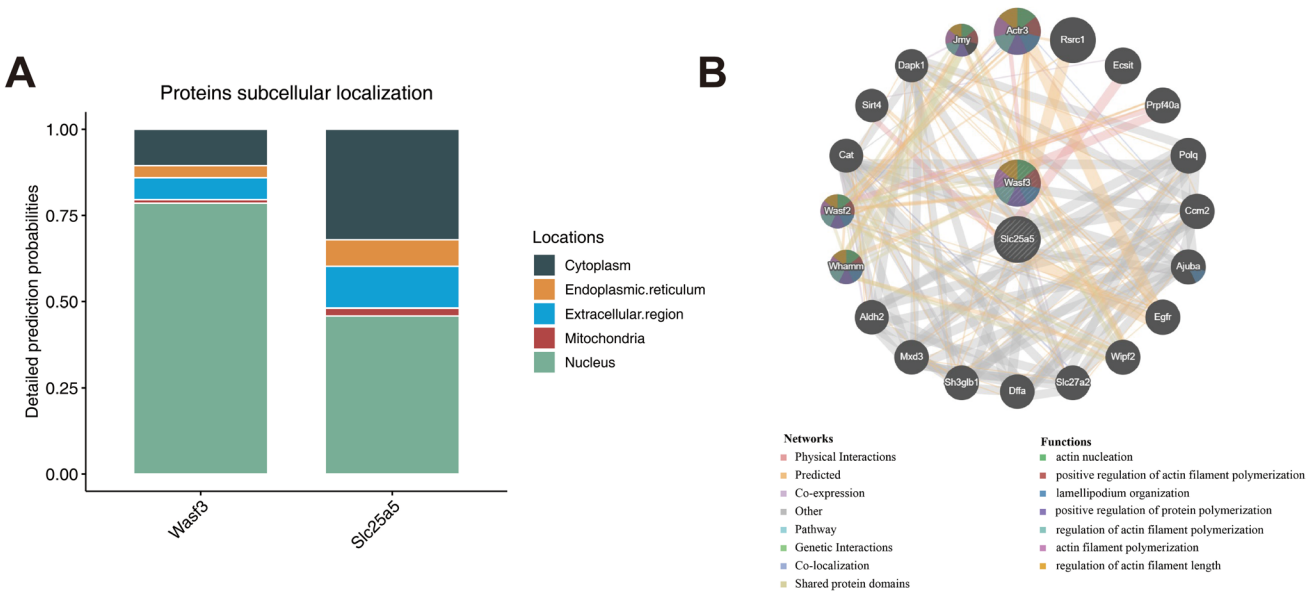

Fig. 3 Localization and gene relationships of key products (Wasf3 and Slc25a5). **A.** Predicted subcellular localization of protein products using mRNALocater; **B.** Gene relationship network diagram based on GeneMANIA biological database

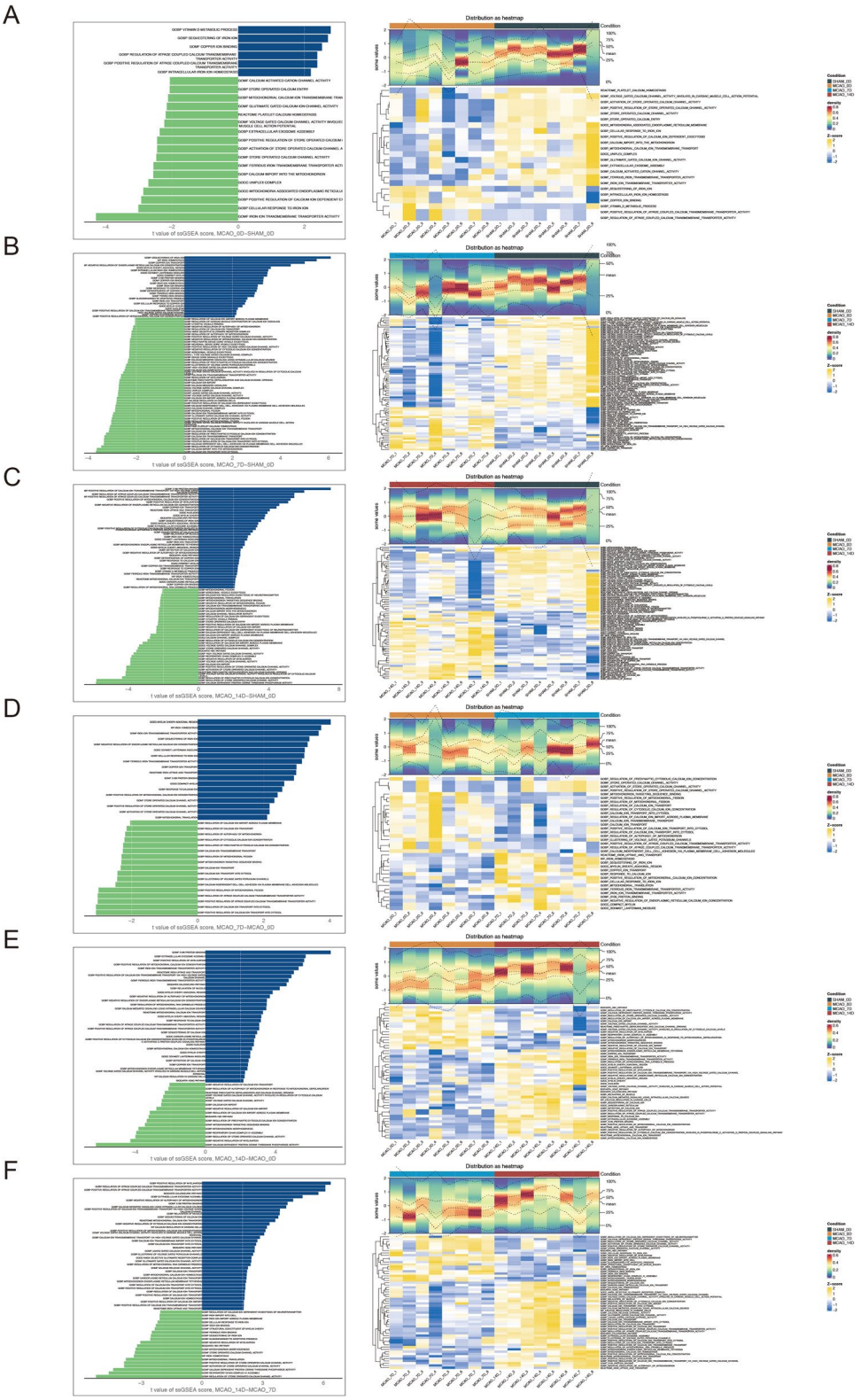

Fig. 4 ssGSEA of differential transcriptomic functions across time points. **A.** Bar chart of difference gene sets function (left) and heat map of ssGSEA scores (right) between MCAO0D and Sham0D; **B.** Bar chart of difference gene sets function (left) and heat map of ssGSEA scores (right) between MCAO7D and Sham0D; **C.** Bar chart of difference gene sets function (left) and heat map of ssGSEA scores (right) between MCAO14D and Sham0D; **D.** Bar chart of difference gene sets function (left) and heat map of ssGSEA scores (right) between MCAO7D and MCAO0D; **E.** Bar chart of difference gene sets function (left) and heat map of ssGSEA scores (right) between MCAO14D and MCAO0D; **F.** Bar chart of difference gene sets function (left) and heat map of ssGSEA scores (right) between MCAO14D and MCAO7D

metabolism by cycling ADP and ATP across mitochondrial membranes (Frank et al. 2004). Beyond its role in bioenergetics, Yao et al. recently demonstrated that *Slc25a5* modulates mitochondrial calcium signaling, exacerbating neuronal apoptosis in cerebral ischemia–reperfusion models (Yao et al. 2023). In this study, our multi-omics data revealed that both genes exhibited transient downregulation immediately post-IS, followed by gradual recovery over 14 days.

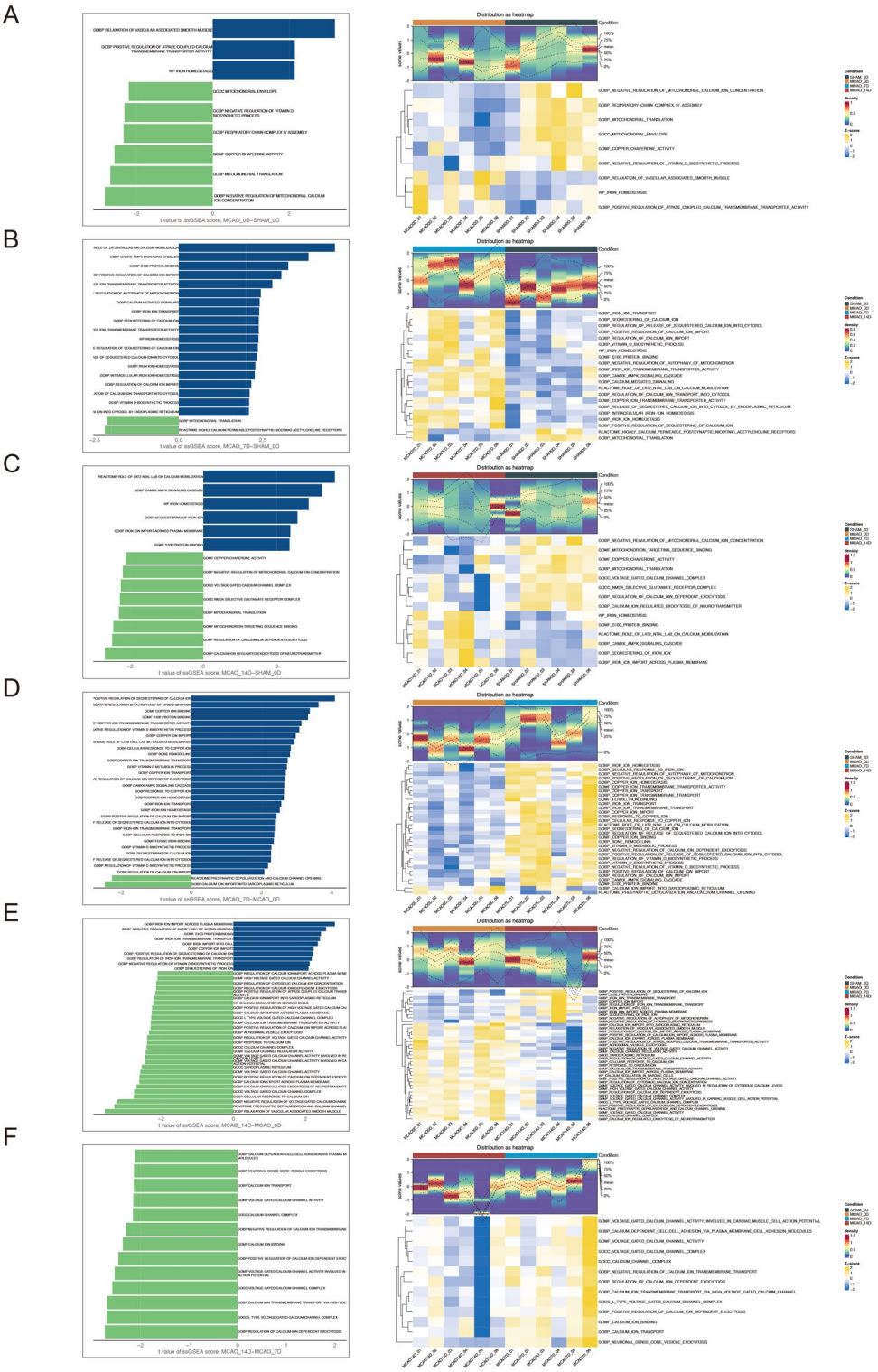

Fig. 5 ssGSEA of differential proteomic functions across time points. **A.** Bar chart of difference gene sets function (left) and heat map of ssGSEA scores (right) between MCAO0D and Sham0D; **B.** Bar chart of difference gene sets function (left) and heat map of ssGSEA scores (right) between MCAO7D and Sham0D; **C.** Bar chart of difference gene sets function (left) and heat map of ssGSEA scores (right) between MCAO14D and Sham0D; **D.** Bar chart of difference gene sets function (left) and heat map of ssGSEA scores (right) between MCAO7D and MCAO0D; **E.** Bar chart of difference gene sets function (left) and heat map of ssGSEA scores (right) between MCAO14D and MCAO0D; **F.** Bar chart of difference gene sets function (left) and heat map of ssGSEA scores (right) between MCAO14D and MCAO7D

Experimental validation confirmed reduced mRNA and protein levels at day 7, with *Wasf3* showing significant suppression ($p < 0.01$). To our knowledge, this is the first study to implicate *Wasf3* and *Slc25a5* in IS pathogenesis using an MCAO model, positioning them as potential biomarkers for disease progression. However, their precise mechanisms, particularly in myelin repair, remain undefined. Future studies should explore whether their dynamic expression reflects compensatory remodeling or persistent dysfunction, and how these pathways intersect with neuroinflammation and oxidative stress.

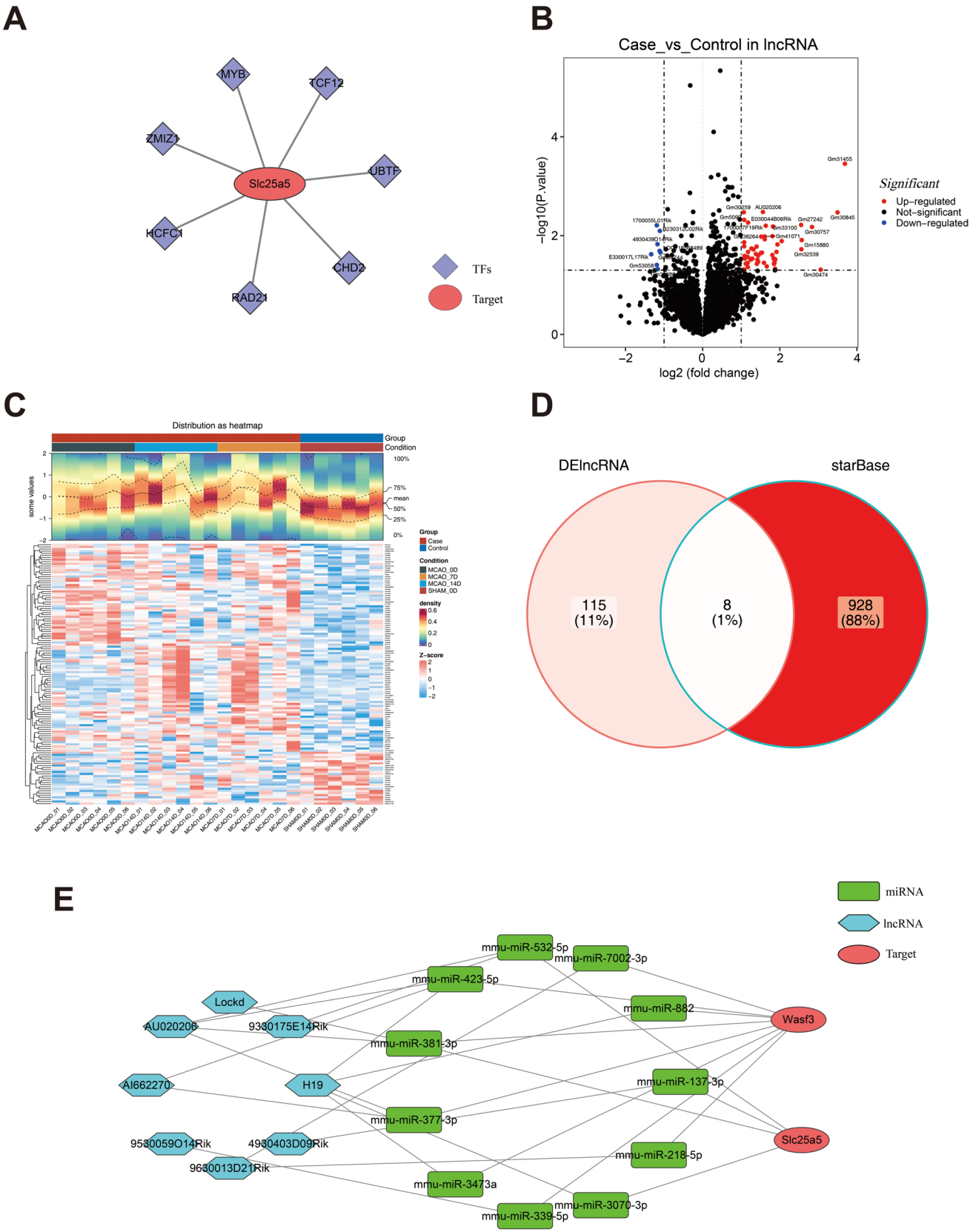
A
MYB
TCF12
ZMIZ1
Slc25a5
UBTF
HCFC1
CHD2
RAD21
TFs
Target
B
Case_vs_Control in lncRNA
−log10(P.value)
log2 (fold change)
Significant
Up−regulated
Not−significant
Down−regulated
C
Distribution as heatmap
Group
Condition
some values
Case
Control
MCAO_0D
MCAO_7D
MCAO_14D
SHAM_0D
density
Z−score
D
DEIncRNA
starBase
115
(11%)
8
(1%)
928
(88%)
E
miRNA
lncRNA
Target
mmu-miR-532-5p
mmu-miR-7002-3p
mmu-miR-423-5p
Lockd
mmu-miR-882
AU020206
9330175E14Rik
Wasf3
mmu-miR-381-3p
AI662270
H19
mmu-miR-137-3p
mmu-miR-377-3p
9530059O14Rik
4930403D09Rik
Slc25a5
mmu-miR-218-5p
9630013D21Rik
mmu-miR-3473a
mmu-miR-3070-3p
mmu-miR-339-5p

◂**Fig. 6** Construction of lncRNA-miRNA-mRNA regulatory networks. **A.** Transcription factor (TF)-mRNA regulatory network; Purple diamonds represented transcription factors and orange ovals indicated key genes; **B.** Volcano plot of differential lncRNA expression between MCAO and Sham groups: red dots indicate upregulated genes, blue dots indicate downregulated genes, and black dots represent genes with no significant difference; **C.** Heatmap of differential lncRNA expression between two groups, where each small square represents a gene, with color intensity reflecting the Z-score of gene expression after sample normalization (the color intensity becomes red with higher expression levels and blue with lower expression levels); **D.** Intersection of key gene-related lncRNAs and differential lncRNAs predicted by Starbase; **E.** Prediction of mRNA-miRNA-lncRNA regulatory networks; green represented miRNAs, blue represented lncRNAs, and red represented key genes

To delineate the temporal dynamics of post-ischemic metabolic and functional alterations, ssGSEA was employed to assess immunoregulation, exosome activity, mitochondrial function, and copper–iron–calcium ion metabolism across groups stratified by stroke onset time. Transcriptomic profiling of the MCAO0D vs. Sham0D comparison revealed early metabolic disruptions: suppression of vitamin D biosynthesis, copper chaperone activity, and respiratory chain complex IV components, alongside enhanced iron homeostasis and ATPase-coupled calcium transporter activity. Parallel proteomic analysis corroborated these findings, showing reduced ferric transmembrane transport and calcium channel activation, but elevated iron chelation, vitamin D metabolism, and copper ion binding post-MCAO. Integrating these results with prior evidence, we propose that *Wasf3* and *Slc25a5*, previously linked to mitochondrial respiration and calcium signaling (Frank et al. 2004; Suetsugu et al. 1999; Wang et al. 2023; Yao et al. 2023), modulate actin and protein polymerization via metabolic crosstalk. These findings advance our understanding of myelin pathology in IS and highlight novel therapeutic targets. This hypothesis aligns with studies demonstrating that copper chaperones enhance Cu/Zn superoxide dismutase activity, mitigating oxidative neuronal death (Choi et al. 2005) and that iron homeostasis safeguards against oxidative stress while its dysregulation exacerbates tissue injury (Naito et al. 2013). Notably, iron's dual role as an enzymatic cofactor in myelination and energy production (Wu et al. 2023) underscores its centrality to post-stroke recovery. These findings position *Wasf3* and *Slc25a5* as critical regulators of copper-iron crosstalk, modulating redox homeostasis to maintain cellular integrity during ischemic injury. By elucidating their role in balancing metal ion metabolism, this study bridges molecular mechanisms to therapeutic strategies, offering a foundation for investigating copper- and iron-targeted interventions in neuroprotection and ischemic stroke treatment. Such insights could pave the way for novel therapeutic avenues that harness metal ion regulation to mitigate oxidative damage and enhance recovery post-stroke.

This study elucidates the regulatory mechanisms of IS biomarkers through the construction of a competing endogenous RNA (ceRNA) network, revealing critical pathways linking apoptosis and myelin dysfunction post-IS. A central node in this network, lncRNA-H19, a highly conserved and developmentally regulated transcript, emerged as a key modulator of neuroinflammation and apoptosis (Pope et al. 2017). Wang et al. demonstrated that H19 exacerbates NLRP3/6 inflammasome dysregulation, driving cytokine overproduction and neuronal death, effects reversed by H19 knockout (Wan et al. 2020). Beyond inflammation, H19 recruits transcription factors like FOXO1 to regulate transcriptional programs governing cellular proliferation, autophagy, and oxidative stress (Li et al. 2018; Xing et al. 2018), while mitochondrial dysfunction further activates H19-mediated caspase-dependent apoptotic signaling (Wan et al. 2020). These findings align with our multi-omics data, which position H19 as a nexus connecting mitochondrial regulation (*Wasf3*/*Slc25a5*) to inflammatory and cytoskeletal remodeling pathways. The ceRNA network also highlights miRNAs with conserved roles in injury response. For instance, mmu-miR-423-5p, a stress-responsive miRNA implicated in inflammation and tissue repair (J. Li et al. 2022a, b, c; Yang et al. 2023), forms a regulatory axis with *Wasf3* and H19 (*Wasf3–mmu-miR-423-5p–H19*). This axis modulates actin nucleation, filament polymerization, and lamellipodium dynamics in neurons and oligodendrocytes, processes critical for myelination and structural plasticity. Conversely, suppression of miR-137-3p, shown to enhance hepatic stellate cell proliferation and repair (Yang et al. 2021), suggests divergent miRNA roles in post-IS recovery. KEGG/GO analyses further corroborate these findings, with gene functions converging on myelination, myelin assembly, and structural integrity of central/peripheral nervous system myelin sheaths. These findings confirm the regulatory mechanisms of biomarkers and the constructed ceRNA network, underscoring the critical roles of *Wasf3* and *Slc25a5* in the onset and progression of IS. This identifies novel therapeutic targets and strategies for future research, particularly in IS treatment, with significant potential for clinical translation.

Myelin loss, exceeding axon loss in the area surrounding the infarction, has been observed in a mouse model of white matter stroke, highlighting an opportunity to mitigate axonal damage through myelin regeneration (Khodanovich et al. 2021). Screening 362 compounds via the Comparative Toxicogenomics Database (CTD) identified VPA, a branched short-chain fatty acid used clinically for epilepsy, as the top candidate interacting with the key myelin-related genes *Wasf3* and *Slc25a5*. Molecular docking revealed strong binding affinity between VPA and proteins encoded by these genes. Beyond its established role in modulating neuronal excitability through

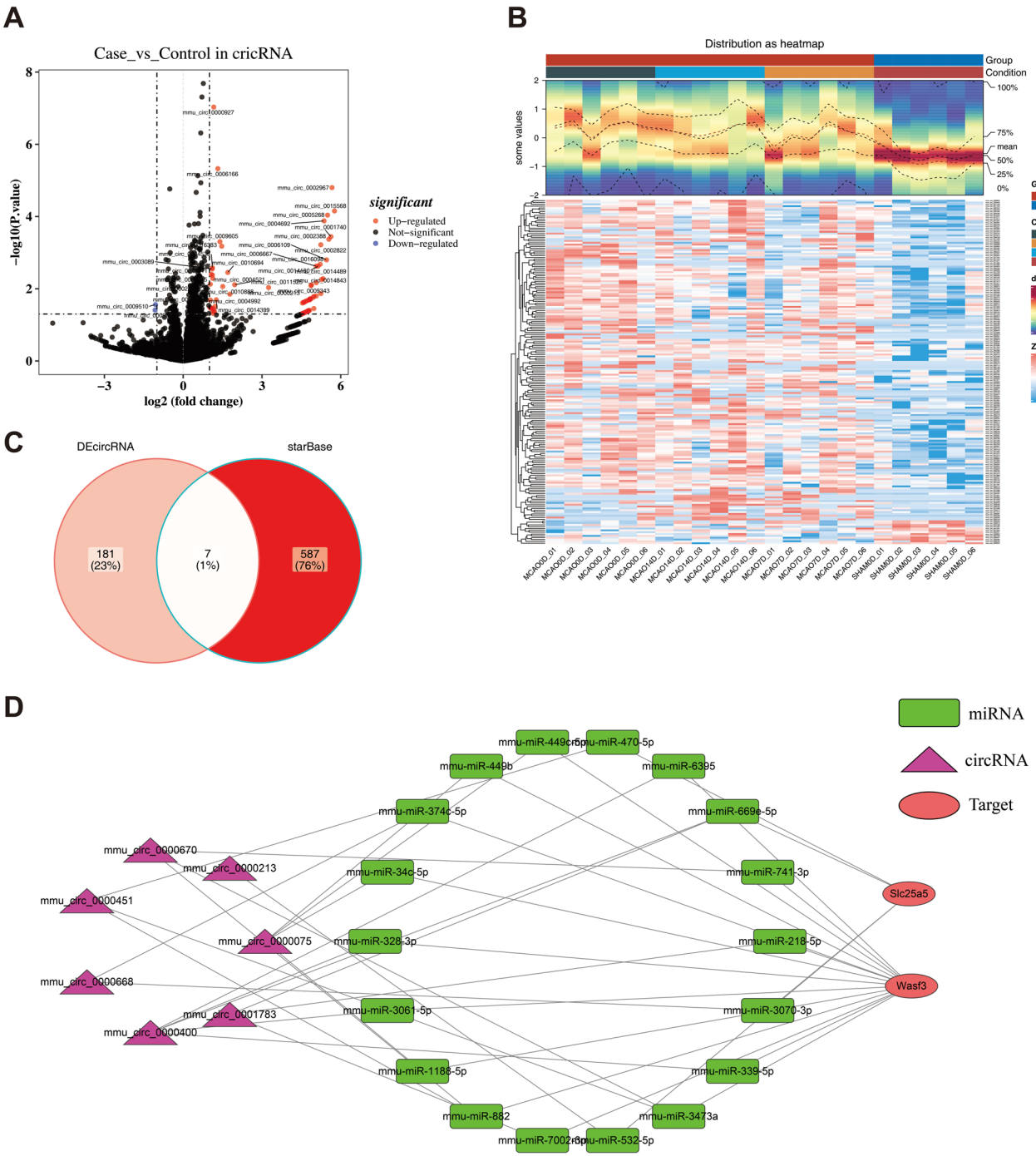

Fig. 7 Construction of circRNA-miRNA-mRNA regulatory networks. **A.** Volcano plot of differential circRNA expression between MCAO and Sham groups: red dots indicate upregulated genes, blue dots indicate downregulated genes, and black dots represent genes with no significant difference; **B.** Heatmap of differential circRNA expression between two groups; red indicated high expression, blue indicated low expression; **C.** Intersection of key gene-related circRNAs and differential circRNAs predicted by Starbase; **D.** Prediction of mRNA-miRNA-circRNA transcriptional regulatory networks; green represented miRNA, purple represented circRNA, and red represented key genes

calcium/potassium channel regulation (Mishra et al. 2021; Zhu et al. 2017). VPA interacts with mitochondrial N-acetylglutamate synthase (Aires et al. 2011) and demonstrates neuroprotective effects post-stroke, including

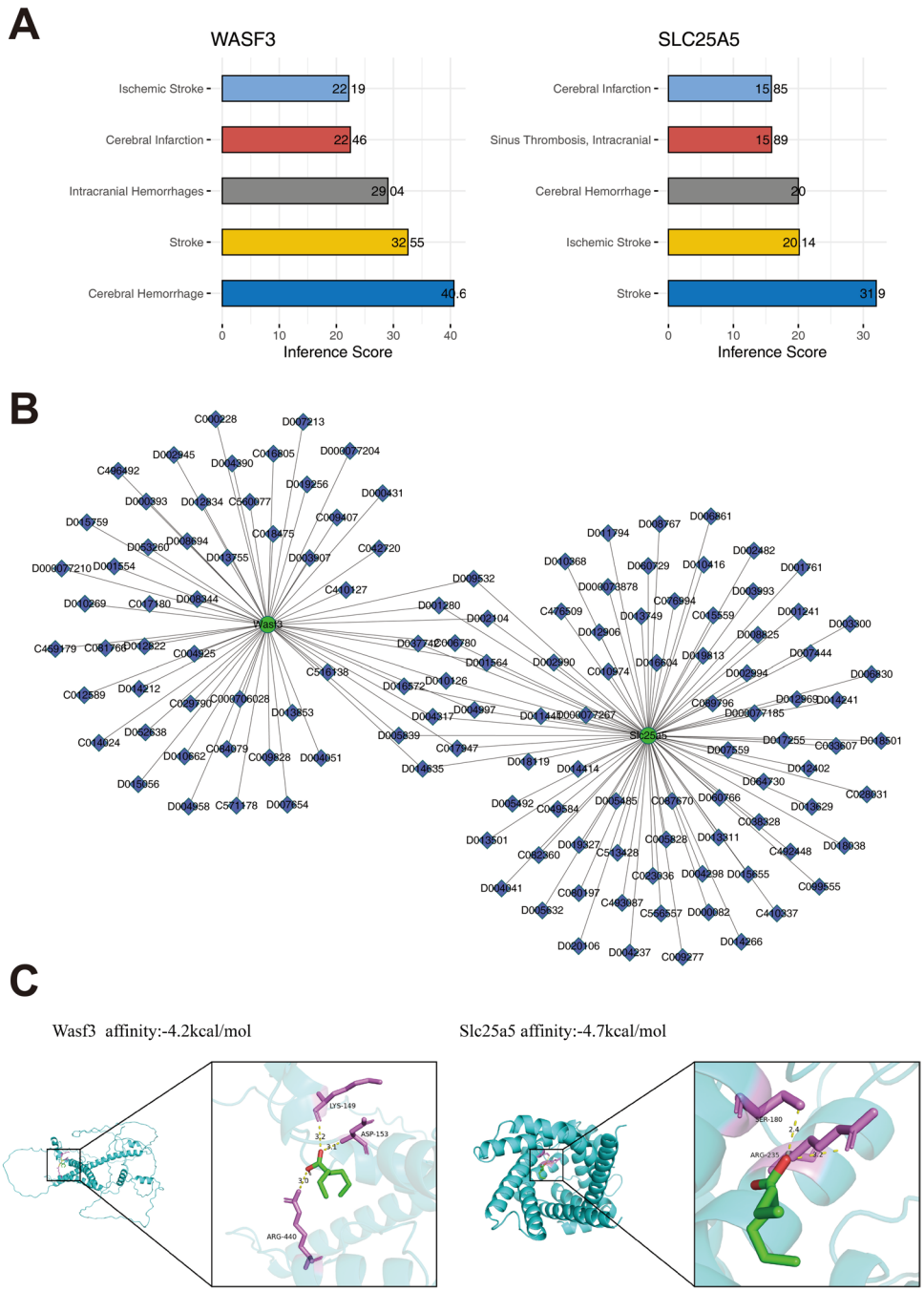

Fig. 8 Analysis of key genes in other cerebrovascular diseases and drug prediction. **A.** Interaction scores between Wasf3 and Slc25a5 and the top five diseases, predicted by CTD; **B.** Drug prediction network related to key genes, constructed using CTD; green circles were key genes, blue diamonds were drug small molecules; **C.** Conformation of Valproic Acid binding to the two key genes with the lowest binding energy

suppression of glial scar formation (Gao et al. 2022) and upregulation of extracellular matrix remodeling genes in peri-infarct regions (Kuo et al. 2021). To the best of our knowledge, the protective effect of VPA on the white matter has not yet been clarified. This study newly posits that VPA enhances neuroprotection and myelin repair by binding to *Wasf3* and *Slc25a5*, thereby regulating calcium metabolism, mitochondrial respiration, and actin filament dynamics. These findings offer novel insights into pharmacological strategies targeting white matter in IS patients. If future clinical studies validate the efficacy and safety of VPA in white matter repair, it may emerge as a promising therapeutic approach for myelin regeneration in IS. Further clinical and experimental investigations are warranted to confirm the utility of *Wasf3* and *Slc25a5* as biomarkers for IS diagnosis and prognosis.

Table 1 Demonstration of the binding energies in molecular docking of Valproic Acid (VPA) and the two key genes

Molecule_name	Gene_name	PDB ID	Energy (kcal/mol)
Valproic Acid	Wasf3	AF-Q8VHI6-F1	−4.2
Valproic Acid	Slc25a5	AF-P51881-F1	−4.7

Limitations

This study has several limitations. First, while the C57BL/6 mouse model is widely used, its results may not fully recapitulate human pathophysiology, potentially limiting the generalizability of our findings. Future validation in diverse animal models and clinical cohorts is warranted. Second, the lack of significant changes in *Slc25a5* expression in qRT-PCR and WB analyses may stem from an insufficient sample size or reliance on β-actin as the sole housekeeping gene for normalization. Incorporating multiple reference genes and expanding sample sizes in future studies could enhance data reliability and clarify *Slc25a5*'s biomarker potential. Third, although key MRGs were identified, their functional roles in post-IS pathology remain unvalidated. Follow-up experiments, such as gene knockout or overexpression, are needed to confirm their mechanistic contributions. Finally, while bioinformatics predictions highlight VPA as a therapeutic candidate, its neuroprotective efficacy and safety require rigorous preclinical and clinical testing. Additional investigations should assess VPA's standalone and combinatorial effects with existing myelin repair strategies. Despite these limitations, our findings provide valuable insights into IS pathophysiology and lay a foundation for future research to refine diagnostic and therapeutic approaches.

Conclusion

This study employed integrated transcriptomic and proteomic analyses to identify two key MRGs, *Wasf3* and *Slc25a5*, implicated in the pathophysiology of IS. By combining bioinformatics tools, we elucidated their roles in mitochondrial respiration, calcium metabolism, and cytoskeletal dynamics, while mapping their regulatory networks through ceRNA and transcription factor interactions. Our findings not only advance the understanding of post-IS myelin pathology but also lay the groundwork for developing targeted therapies. The discovery of VPA as a high-affinity binder for *Wasf3* and *Slc25a5* highlights its potential to modulate these pathways, offering a novel strategy to enhance myelin regeneration and functional recovery. The properties position VPA as a promising candidate for repurposing in stroke therapy. Moving forward, preclinical and clinical studies are essential to validate the therapeutic efficacy of VPA and refine MRG-targeted interventions. By bridging molecular mechanisms to translational applications, this work underscores the transformative potential of multi-omics approaches in overcoming the limitations of conventional stroke therapies.

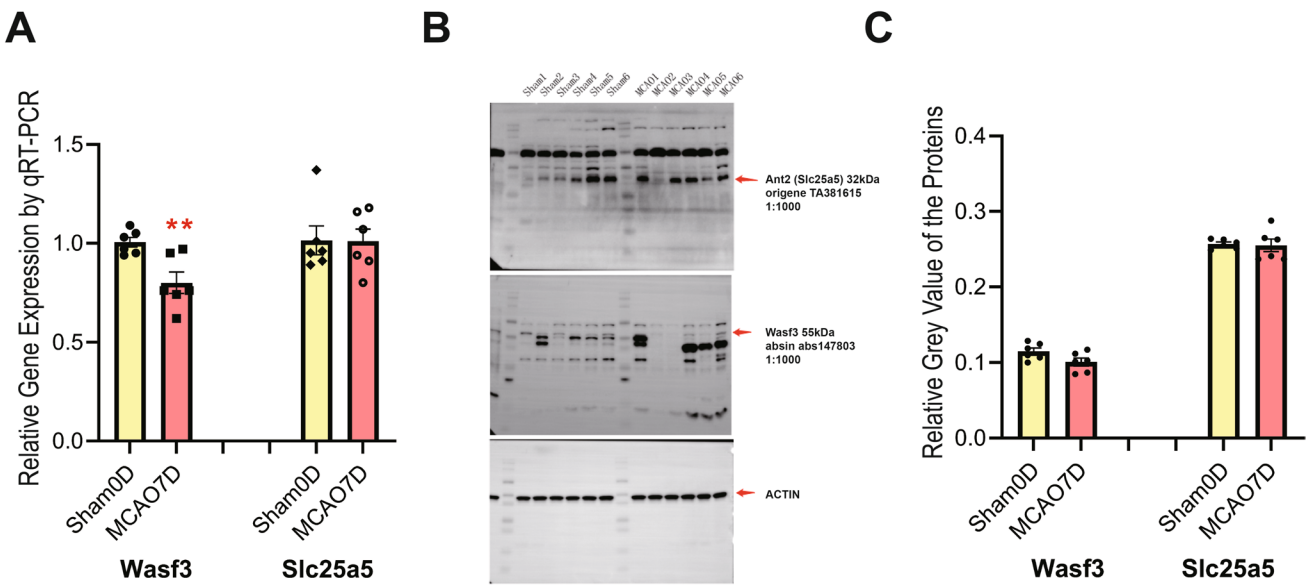

Fig. 9 Validation of expression level differences of key genes in ischemic stroke and control groups. **A.** Comparison of relative gene expression of Wasf3 and Slc25a5 between Sham0D and MCAO7D groups; **B.** Comparison of protein expression levels between Sham0D and MCAO7D samples; **C.** Comparison of relative gray values of Wasf3 and Slc25a5 protein expression

Supplementary Information The online version contains supplementary material available at https://doi.org/10.1007/s10142-025-01573-6.

Acknowledgements We acknowledge the help of all of our colleagues in the Department of Rehabilitation Medicine of Longhua People's Hospital without whom this study would not have been possible.

Authors contribution Qiuyang Qian and Hao Lyu contributed equally in project design, animal model operation and manuscript drafting. Wei Wang, Qiwen Wang and Desheng Li helped with experimental operation and analyzed the data. Xiaojia Liu and Yi He revised the manuscript and designed two figures. Mei Shen wrote and revised the manuscript, including designing the figures and tables.

Funding This work was supported by the Shenzhen Science and Technology Program (Grant No.RCBS20210609104401012 and Grant No.JCYJ20220530165207017) and the Scientific Research Projects of Medical and Health Institutions of Longhua District, Shenzhen (Grant No.2022073).

Data availability The data that support the findings of this study are available to access from the following public database: The transcriptome data has been uploaded to the NCBI SRA platform, Accession Code: PRJNA1105125, https://www.ncbi.nlm.nih.gov/sra/PRJNA1105125. The mass spectrometry proteomics data have been deposited to the ProteomeXchange Consortium (https://proteomecentral.proteomexchange.org) via the iProX partner repository with the dataset identifier PXD051812.

Declarations

Competing interests The authors declare no competing interests.

References

Aires CC, van Cruchten A, Ijlst L, de Almeida IT, Duran M, Wanders RJ, Silva MF (2011) New insights on the mechanisms of valproate-induced hyperammonemia: inhibition of hepatic N-acetylglutamate synthase activity by valproyl-CoA. J Hepatol 55(2):426–434. https://doi.org/10.1016/j.jhep.2010.11.031

Bae JH, Gong ZY, Guo A, Laporte JP, Faulkner ME, Bouhrara M (2025) PhysicOmics: combining MR physics, proteomics, and transcriptomics to study cerebral aging and neurodegeneration. ALZH DEMENT-DADM 20(S9):e093695. https://doi.org/10.1002/alz.093695

Chen M, Lyu H, Li T, Su XW, Leung CK, Xiong MZQ, Poon WS, Cai YF, Lu G, Chan WY, Wang LX (2020) Study of the association between gait variability and gene expressions in a mouse model of transient focal ischemic stroke. Int J Neurosci 130(1):52–63. https://doi.org/10.1080/00207454.2019.1663188

Choi SH, Kim DW, Kim SY, An JJ, Lee SH, Choi HS, Sohn EJ, Hwang SI, Won MH, Kang TC, Kwon HJ, Kang JH, Cho SW, Park J, Eum WS, Choi SY (2005) Transduced human copper chaperone for Cu, Zn-SOD (PEP-1-CCS) protects against neuronal cell death. Mol Cells 20(3):401–408

Chung RH, Kang CY (2019) A multi-omics data simulator for complex disease studies and its application to evaluate multi-omics data analysis methods for disease classification. Gigascience 8(5). https://doi.org/10.1093/gigascience/giz045

Corbetta M, Siegel JS, Shulman GL (2018) On the low dimensionality of behavioral deficits and alterations of brain network connectivity after focal injury. Cortex 107:229–237. https://doi.org/10.1016/j.cortex.2017.12.017

Du H, Xu Y, Zhu L (2022) Role of semaphorins in ischemic stroke. Front Mol Neurosci 15:848506. https://doi.org/10.3389/fnmol.2022.848506

Edwards D, Williams J, Carrier J, Davies J (2022) Technologies used to facilitate remote rehabilitation of adults with deconditioning, musculoskeletal conditions, stroke, or traumatic brain injury: an umbrella review. JBI Evid Synth 20(8):1927–1968. https://doi.org/10.11124/jbies-21-00241

Frank M, Egile C, Dyachok J, Djakovic S, Nolasco M, Li R, Smith LG (2004) Activation of Arp2/3 complex-dependent actin polymerization by plant proteins distantly related to Scar/WAVE. Proc Natl Acad Sci U S A 101(46):16379–16384. https://doi.org/10.1073/pnas.0407392101

Futschik ME, Carlisle B (2005) Noise-robust soft clustering of gene expression time-course data. J Bioinform Comput Biol 3(4):965–988. https://doi.org/10.1142/s0219720005001375

Gao X, Zeb S, He YY, Guo Y, Zhu YM, Zhou XY, Zhang HL (2022) Valproic acid inhibits glial scar formation after ischemic stroke. Pharmacology 107(5–6):263–280. https://doi.org/10.1159/000514951

Ghosh D, Bernstein JA, Khurana Hershey GK, Rothenberg ME, Mersha TB (2018) Leveraging multilayered "Omics" data for atopic dermatitis: a road map to precision medicine. Front Immunol 9:2727. https://doi.org/10.3389/fimmu.2018.02727

Gu Z, Eils R, Schlesner M (2016) Complex heatmaps reveal patterns and correlations in multidimensional genomic data. Bioinformatics 32(18):2847–2849. https://doi.org/10.1093/bioinformatics/btw313

Guo Z, Qian Q, Wong K, Zhu H, Huang Y, Hu X, Zheng Y (2020) Altered Corticomuscular Coherence (CMCoh) pattern in the upper limb during finger movements after stroke. Front Neurol 11:410. https://doi.org/10.3389/fneur.2020.00410

Hänzelmann S, Castelo R, Guinney J (2013) GSVA: gene set variation analysis for microarray and RNA-seq data. BMC Bioinformatics 14:7. https://doi.org/10.1186/1471-2105-14-7

Hochrainer K, Yang W (2022) Stroke proteomics: from discovery to diagnostic and therapeutic applications. Circ Res 130(8):1145–1166. https://doi.org/10.1161/circresaha.122.320110

Khodanovich MY, Gubskiy IL, Kudabaeva MS, Namestnikova DD, Kisel AA, Anan'ina TV, Tumentceva YA, Mustafina LR, Yarnykh VL (2021) Long-term monitoring of chronic demyelination and remyelination in a rat ischemic stroke model using macromolecular proton fraction mapping. J Cereb Blood Flow Metab 41(11):2856–2869. https://doi.org/10.1177/0271678x211020860

Kuo TT, Wang V, Wu JS, Chen YH, Tseng KY (2021) Post-stroke delivery of valproic acid promotes functional recovery and differentially modifies responses of peri-infarct microglia. Front Mol Neurosci 14:639145. https://doi.org/10.3389/fnmol.2021.639145

Li C, Zhang T, Yu K, Xie H, Bai Y, Zhang L, Wu Y, Wang N (2017) Neuroprotective effect of electroacupuncture and upregulation of

hypoxia-inducible factor-1α during acute ischaemic stroke in rats. Acupunct Med 35(5):360–365. https://doi.org/10.1136/acupmed-2016-011148

Li M, Zhao Y, Zhan Y, Yang L, Feng X, Lu Y, Lei J, Zhao T, Wang L, Zhao H (2020) Enhanced white matter reorganization and activated brain glucose metabolism by enriched environment following ischemic stroke: Micro PET/CT and MRI study. Neuropharmacology 176:108202. https://doi.org/10.1016/j.neuropharm.2020.108202

Li J, Shen Z, Chen W, Feng Z, Fang L, Zhao J, Liu C, Du J, Cheng Y (2022a) Screening of miRNAs in white blood cell as a radiation biomarkers for rapid assessment of acute radiation injury. Dose Response 20(3):15593258221123680. https://doi.org/10.1177/15593258221123679

Li W, Shao C, Zhou H, Du H, Chen H, Wan H, He Y (2022b) Multi-omics research strategies in ischemic stroke: A multidimensional perspective. Ageing Res Rev 81:101730. https://doi.org/10.1016/j.arr.2022.101730

Li Y, Liu Z, Song Y, Pan JJ, Jiang Y, Shi X, Liu C, Ma Y, Luo L, Mamtilahun M, Shi Z, Khan H, Xie Q, Wang Y, Tang Y, Zhang Z, Yang GY (2022c) M2 microglia-derived extracellular vesicles promote white matter repair and functional recovery via miR-23a-5p after cerebral ischemia in mice. Theranostics 12(7):3553–3573. https://doi.org/10.7150/thno.68895

Li DY, Busch A, Jin H, Chernogubova E, Pelisek J, Karlsson J, Sennblad B, Liu S, Lao S, Hofmann P, Bäcklund A, Eken SM, Roy J, Eriksson P, Dacken B, Ramanujam D, Dueck A, Engelhardt S, Boon, RA, ..., Maegdefessel L (2018) H19 Induces Abdominal Aortic Aneurysm Development and Progression. Circulation 138(15):1551–1568. https://doi.org/10.1161/circulationaha.117.032184

Love MI, Huber W, Anders S (2014) Moderated estimation of fold change and dispersion for RNA-seq data with DESeq2. Genome Biol 15(12):550. https://doi.org/10.1186/s13059-014-0550-8

Meng S, Wang B, Li W (2023) LncRNA MALAT1 improves cerebral ischemia-reperfusion injury and cognitive dysfunction by regulating miR-142-3p/SIRT1 axis. Int J Neurosci 133(7):740–753. https://doi.org/10.1080/00207454.2021.1972999

Mishra MK, Kukal S, Paul PR, Bora S, Singh A, Kukreti S, Saso L, Muthusamy K, Hasija Y, Kukreti R (2021) Insights into structural modifications of valproic acid and their pharmacological profile. Molecules 27(1). https://doi.org/10.3390/molecules27010104

Montaner J, Ramiro L, Simats A, Tiedt S, Makris K, Jickling GC, Debette S, Sanchez JC, Bustamante A (2020) Multilevel omics for the discovery of biomarkers and therapeutic targets for stroke. Nat Rev Neurol 16(5):247–264. https://doi.org/10.1038/s41582-020-0350-6

Naito Y, Sawada H, Oboshi M, Fujii A, Hirotani S, Iwasaku T, Okuhara Y, Eguchi A, Morisawa D, Ohyanagi M, Tsujino T, Masuyama T (2013) Increased renal iron accumulation in hypertensive nephropathy of salt-loaded hypertensive rats. PLoS ONE 8(10):e75906. https://doi.org/10.1371/journal.pone.0075906

Paul S, Candelario-Jalil E (2021) Emerging neuroprotective strategies for the treatment of ischemic stroke: An overview of clinical and preclinical studies. Exp Neurol 335:113518. https://doi.org/10.1016/j.expneurol.2020.113518

Pope C, Piekos SC, Chen L, Mishra S, Zhong XB (2017) The role of H19, a long non-coding RNA, in mouse liver postnatal maturation. PLoS ONE 12(11):e0187557. https://doi.org/10.1371/journal.pone.0187557

Raffaele S, Fumagalli M (2022) Dynamics of microglia activation in the ischemic brain: implications for myelin repair and functional recovery. Front Cell Neurosci 16:950819. https://doi.org/10.3389/fncel.2022.950819

Ritchie ME, Phipson B, Wu D, Hu Y, Law CW, Shi W, Smyth GK (2015) limma powers differential expression analyses for RNA-sequencing and microarray studies. Nucleic Acids Res 43(7):e47. https://doi.org/10.1093/nar/gkv007

Robin X, Turck N, Hainard A, Tiberti N, Lisacek F, Sanchez JC, Müller M (2011) pROC: an open-source package for R and S+ to analyze and compare ROC curves. BMC Bioinformatics 12:77. https://doi.org/10.1186/1471-2105-12-77

Rojahn TB, Vorstandlechner V, Krausgruber T, Bauer WM, Alkon N, Bangert C, Thaler FM, Sadeghyar F, Fortelny N, Gernedl V, Rindler K, Elbe-Bürger A, Bock C, Mildner M, Brunner PM (2020) Single-cell transcriptomics combined with interstitial fluid proteomics defines cell type-specific immune regulation in atopic dermatitis. J Allergy Clin Immunol 146(5):1056–1069. https://doi.org/10.1016/j.jaci.2020.03.041

Singh RE, Iqbal K, White G, Hutchinson TE (2018) A Systematic review on muscle synergies: from building blocks of motor behavior to a neurorehabilitation tool. Appl Bionics Biomech 2018:3615368. https://doi.org/10.1155/2018/3615368

Song Y, Yang L, Han Y, Li W, Wei T, Gao Y, Hu Q, Li H, Sun Y (2025) Transcriptomics and Proteomics Analysis of the Liver of RAD52 Knockout Mice. Int J Mol Sci 26(1). https://doi.org/10.3390/ijms26010339

Stefancin P, Govindarajan ST, Krupp L, Charvet L, Duong TQ (2019) Resting-state functional connectivity networks associated with fatigue in multiple sclerosis with early age onset. Mult Scler Relat Disord 31:101–105. https://doi.org/10.1016/j.msard.2019.03.020

Suetsugu S, Miki H, Takenawa T (1999) Identification of two human WAVE/SCAR homologues as general actin regulatory molecules which associate with the Arp2/3 complex. Biochem Biophys Res Commun 260(1):296–302. https://doi.org/10.1006/bbrc.1999.0894

Trott O, Olson AJ (2010) AutoDock Vina: improving the speed and accuracy of docking with a new scoring function, efficient optimization, and multithreading. J Comput Chem 31(2):455–461. https://doi.org/10.1002/jcc.21334

Veldsman M, Curwood E, Pathak S, Werden E, Brodtmann A (2018) Default mode network neurodegeneration reveals the remote effects of ischaemic stroke. J Neurol Neurosurg Psychiatry 89(3):318–320. https://doi.org/10.1136/jnnp-2017-315676

Wan P, Su W, Zhang Y, Li Z, Deng C, Li J, Jiang N, Huang S, Long E, Zhuo Y (2020) LncRNA H19 initiates microglial pyroptosis and neuronal death in retinal ischemia/reperfusion injury. Cell Death Differ 27(1):176–191. https://doi.org/10.1038/s41418-019-0351-4

Wang J, Wu N, Feng X, Liang Y, Huang M, Li W, Hou L, Yin C (2022) PROS1 shapes the immune-suppressive tumor microenvironment and predicts poor prognosis in glioma. Front Immunol 13:1052692. https://doi.org/10.3389/fimmu.2022.1052692

Wang PY, Ma J, Kim YC, Son AY, Syed AM, Liu C, Mori MP, Huffstutler RD, Stolinski JL, Talagala SL, Kang JG, Walitt BT, Nath A, Hwang PM (2023) WASF3 disrupts mitochondrial respiration and may mediate exercise intolerance in myalgic encephalomyelitis/chronic fatigue syndrome. Proc Natl Acad Sci U S A 120(34):e2302738120. https://doi.org/10.1073/pnas.2302738120

Wu T, Hu E, Xu S, Chen M, Guo P, Dai Z, Feng T, Zhou L, Tang W, Zhan L, Fu X, Liu S, Bo X, Yu G (2021) clusterProfiler 4.0: a universal enrichment tool for interpreting omics data. Innovation (Camb) 2(3):100141. https://doi.org/10.1016/j.xinn.2021.100141

Wu Q, Ren Q, Meng J, Gao WJ, Chang YZ (2023) Brain iron homeostasis and mental disorders. Antioxidants (Basel) 12(11). https://doi.org/10.3390/antiox12111997

Xie X, Zhang G, Liu N (2024) Comprehensive analysis of abnormal methylation modification differential expression mRNAs between low-grade and high-grade intervertebral disc degeneration and its correlation with immune cells. Ann Med 56(1):2357742. https://doi.org/10.1080/07853890.2024.2357742

Xing YQ, Li A, Yang Y, Li XX, Zhang LN, Guo HC (2018) The regulation of FOXO1 and its role in disease progression. Life Sci 193:124–131. https://doi.org/10.1016/j.lfs.2017.11.030

Yang X, Shu B, Zhou Y, Li Z, He C (2021) Ppic modulates CCl(4)-induced liver fibrosis and TGF-β-caused mouse hepatic stellate cell activation and regulated by miR-137-3p. Toxicol Lett 350:52–61. https://doi.org/10.1016/j.toxlet.2021.06.021

Yang Q, Wang X, Li H, Yin X, Liu H, Hu W, Qing Y, Ding L, Yang L, Li Z, Sun H (2023) Integrative analysis of renal microRNA and mRNA to identify hub genes and pivotal pathways associated with cyclosporine-induced acute kidney injury in mice. Hum Exp Toxicol 42:9603271231215500. https://doi.org/10.1177/09603271231215499

Yao Y, Bade R, Li G, Zhang A, Zhao H, Fan L, Zhu R, Yuan J (2023) Global-scale profiling of differential expressed lysine-lactylated proteins in the cerebral endothelium of cerebral ischemia-reperfusion injury rats. Cell Mol Neurobiol 43(5):1989–2004. https://doi.org/10.1007/s10571-022-01277-6

Yuan Y, Sheng P, Ma B, Xue B, Shen M, Zhang L, Li D, Hou J, Ren J, Liu J, Yan BC, Jiang Y (2023) Elucidation of the mechanism of Yiqi Tongluo Granule against cerebral ischemia/reperfusion injury based on a combined strategy of network pharmacology, multi-omics and molecular biology. Phytomedicine 118:154934. https://doi.org/10.1016/j.phymed.2023.154934

Zhang Q, Chen W, Chen S, Li S, Wei D, He W (2019) Identification of key genes and upstream regulators in ischemic stroke. Brain Behav 9(7):e01319. https://doi.org/10.1002/brb3.1319

Zhu MM, Li HL, Shi LH, Chen XP, Luo J, Zhang ZL (2017) The pharmacogenomics of valproic acid. J Hum Genet 62(12):1009–1014. https://doi.org/10.1038/jhg.2017.91

Zuo M, Guo H, Wan T, Zhao N, Cai H, Zha M, Xiong Y, Xie Y, Ye R, Liu X (2019) Wallerian degeneration in experimental focal cortical ischemia. Brain Res Bull 149:194–202. https://doi.org/10.1016/j.brainresbull.2019.04.023